ALMA Long Baseline Campaigns: Phase Characteristics of Atmosphere at Long Baselines in the Millimeter and Submillimeter Wavelengths

Satoki Matsushita[1],

satoki@asiaa.sinica.edu.tw

Yoshiharu Asaki[2,3], Edward B. Fomalont[2,4], Koh-Ichiro Morita[2,3], Denis Barkats[5], Richard E. Hills[6], Ryohei Kawabe[7,8,9], Luke T. Maud[10], Bojan Nikolic[6], Remo P. J. Tilanus[10], Catherine Vlahakis[4], Nicholas D. Whyborn[2]

ABSTRACT

We present millimeter- and submillimeter-wave phase characteristics measured between 2012 and 2014 of Atacama Large Millimeter/submillimeter Array (ALMA) long baseline campaigns. This paper presents the first detailed investigation of the characteristics of phase fluctuation and phase correction methods obtained with baseline lengths up to $\sim$ 15 km. The basic phase fluctuation characteristics can be expressed with the spatial structure function (SSF). Most of the SSFs show that the phase fluctuation increases as a function of baseline length, with a power-law slope of ~ 0.6. In many cases, we find that the slope becomes shallower (average of $\sim 0.2 - 0.3$) at baseline lengths longer than $\sim$ 1 km, namely showing a turn-over in SSF. These power law slopes do not change with the amount of precipitable water vapor (PWV), but the fitted constants have a weak correlation with PWV, so that the phase fluctuation at a baseline length of 10 km also increases as a function of PWV. The phase correction method using water vapor radiometers (WVRs) works well, especially for the cases where PWV $>$ 1 mm,

[1]Academia Sinica Institute of Astronomy and Astrophysics, P.O. Box 23-141, Taipei 10617, Taiwan, R.O.C.

[2]Joint ALMA Observatory, Alonso de Córdova 3107, Vitacura 763 0355, Santiago, Chile

[3]Chile Observatory, National Astronomical Observatory of Japan, National Institutes of Natural Sciences, Joaquin Montero 3000 Oficina 702, Vitacura, Santiago, C.P.7630409, Chile

[4]National Radio Astronomy Observatory, 520 Edgemont Rd, Charlottesville, VA 22903, USA

[5]Harvard-Smithsonian Center for Astrophysics, 60 Garden St., MS-78, Cambridge, MA 02138, USA

[6]Astrophysics Group, Cavendish Laboratory, University of Cambridge, JJ Thomson Avenue, Cambridge CB3 0HE, UK

[7]National Astronomical Observatory of Japan, 2-21-1 Osawa, Mitaka, Tokyo 181-8588, Japan

[8]Department of Astronomy, School of Science, University of Tokyo, Bunkyo, Tokyo 113-0033, Japan

[9]SOKENDAI (The Graduate University for Advanced Studies), 2-21-1 Osawa, Mitaka, Tokyo 181-8588, Japan

[10]Leiden Observatory, Leiden University, P.O. Box 9513, 2300 RA Leiden, The Netherlands

which reduces the degree of phase fluctuations by a factor of two in many cases. However, phase fluctuations still remain after the WVR phase correction, suggesting the existence of other turbulent constituent that cause the phase fluctuation. This is supported by occasional SSFs that do not exhibit any turn-over; these are only seen when the PWV is low (i.e., when the WVR phase correction works less effectively) or after WVR phase correction. This means that the phase fluctuation caused by this turbulent constituent is inherently smaller than that caused by water vapor. Since in these rare cases there is no turn-over in the SSF up to the maximum baseline length of $\sim$ 15 km, this turbulent constituent must have scale height of 10 km or more, and thus cannot be water vapor, whose scale height is around 1 km. Based on the characteristics, this large scale height turbulent constituent is likely to be water ice or a dry component. Excess path length fluctuation after the WVR phase correction at a baseline length of 10 km is large ($\gtrsim$ 200 μm), which is significant for high frequency ($>$ 450 GHz or $<$ 700 μm) observations. These results suggest the need for an additional phase correction method to reduce the degree of phase fluctuation, such as fast switching, in addition to the WVR phase correction. We simulated the fast switching phase correction method using observations of single quasars, and the result suggests that it works well, with shorter cycle times linearly improving the coherence.

Subject headings: atmospheric effects; site testing; techniques: high angular resolution; techniques: interferometric

1. Introduction

The Atacama Large Millimeter/submillimeter Array (ALMA; Hills et al. 2010) is the world's largest millimeter/submillimeter (mm/submm) interferometer. One of the most important technical developments for ALMA full operation has been making the longest ($\sim$ 15 km) baseline observations possible, which was achieved for the first time at the end of 2014 (ALMA Partnership et al. 2015a).

Prior to that, the longest baseline observations for mm/submm linked arrays had been much shorter, only $\sim$ 2 km at 230 GHz with the Berkeley-Illinois-Maryland Association (BIMA) or the Combined Array for Research in Millimeter-wave Astronomy (CARMA), and several hundred meters at 345 GHz or higher frequencies with the Submillimeter Array (SMA) or the NOrthern Extended Millimeter Array (NOEMA), although there are some very long baseline interferometry (VLBI) observations with the frequency up to 230 GHz and with baseline lengths up to $\sim$ 4000 km (e.g., Doeleman et al. 2008, 2012). The longest baseline length currently possible with ALMA ($\sim$ 15 km), together with a significant increase of the number of baselines (1225 baselines with 50 antennas) compared with the aforementioned mm/submm arrays, is therefore a revolutionary improvement for mm/submm linked arrays. This 15 km baseline length with good *uv* coverage provides milli-arcsecond resolution; such high sensitivity and high fidelity at these wavelengths

cannot be obtained with any other current facilities. Indeed, in the ALMA long baseline campaign in 2014, science verification images revealed extraordinally detailed features of an asteroid (ALMA Partnership et al. 2015b), a protoplanetary disk system (ALMA Partnership et al. 2015c), and a gravitationally lensed system (ALMA Partnership et al. 2015d). In order to continue to improve on the quality of the data, it is important to characterize the atmospheric phase fluctuation, and to test phase correction methods at these long baselines.

Characterization of the atmospheric phase fluctuation so far has mainly been carried out at low frequencies; Very Large Array (VLA) was often used to characterize the atmospheric phase fluctuation at centimeter-wave (cm-wave) with baseline lengths up to a few tens of km (Sramek 1990; Carilli & Holdaway 1999). At higher frequencies, studies with $80 - 230$ GHz ($1 - 3$ mm) are available with baseline lengths up to only about 1 km (Wright 1996; Asaki et al. 1998; Matsushita & Chen 2010). These previous cm-/mm-wave studies displayed similar results for cases where the atmospheric phase fluctuation is caused by water vapor in the atmosphere.

Since 2010, as a part of ALMA Commissioning and Science Verification (CSV), and most recently, as part of the Extension and Optimization of Capabilities (EOC; see ALMA Partnership et al. 2015a), we have conducted several ALMA long baseline campaigns, starting from the longest baseline length of 600 m in 2010 and 2011, 2 km in 2012, 3 km in 2013, and finally $10-15$ km in 2014. In the earlier long baseline campaigns, we mainly conducted basic tests, such as characterizing the phase fluctuation and checking the effectiveness of the WVR phase correction; in the later phase, we mainly concentrated on the coherence time calculation and the evaluation of the fast swtiching phase correction method. Some of the early test results have been reported in Matsushita et al. (2012, 2014, 2016) and Asaki et al. (2012, 2014, 2016), and the overview of the latest $10 - 15$ km baseline test has been reported in ALMA Partnership et al. (2015a).

In this paper, we present the detailed characterization of phase fluctuation, improvement of phase fluctuation after the water vapor radiometer (WVR) phase correction method (Wiedner et al. 2001; Nikolic et al. 2013), coherence time calculation, and the cycle time analysis for the fast switching phase correction method using the data obtained in the ALMA long baseline campaigns. The results presented in this paper replace those reported previously by Matsushita et al. (2012, 2014, 2016). Note that the relation between phase fluctuation and the weather parameters (wind speed, wind direction, temperature, pressure, etc.) will be discussed in the forthcoming paper (Maud et al., in prep.), so that we do not discuss here.

2. Observations and Data Reduction

In this paper, we use the data taken in the long baseline campaigns between 2012 and 2014 (see Sect. A). All the data were taken with observations of a strong point source (i.e., radio-loud quasars) for tens of minutes (usually $10 - 40$ minutes, depending on the longest baseline length) with ~ 1 s integration time per data point. Hereafter we refer to these observations as "single source

stares." For each measurement, ten or more antennas with various baseline lengths have been used. We only used 12 m diameter antenna data and did not use data taken with 7 m diameter antennas in order to make the thermal noise contribution uniform over the data as much as possible.

The single source stares were taken for the purpose of statistical phase analysis beyond the wind crossing time of the longest baseline. For example, assuming (1) a longest baseline length of 10 km, (2) a wind speed along a given baseline of 10 m s^{-1}, and (3) that the phase screen does not change with time (i.e., frozen phase screen; Taylor 1938; Dravskikh & Finkelstein 1979), then the crossing time can be calculated as 1000 s ($\sim$ 17 minutes). To have statistically significant data for the longest baseline data, about twice the measurement time is needed (see Asaki et al. 1996 for the detailed discussion)[11]. We used Bands 3 (100 GHz band), 6 (200 GHz band), and 7 (300 GHz band) for all the campaigns, except for Band 8 (400 GHz band), which was only used in the 2014 campaign.

The data were reduced using the Common Astronomy Software Applications (CASA) package (McMullin et al. 2007), using a standard ALMA calibration prescription. Below we give a brief overview. The WVR phase correction[12] was applied using the program *wvrgcal* (Nikolic et al. 2012) installed inside CASA. The precipitable water vapor (PWV) values calculated by *wvrgcal* is used as a measure of the water vapor content in front of the array of each data set.

Linear phase drift, which is mostly caused by the antenna position determination error (main reason for this error is due to poor knowledge of the dry air delay term for each antenna, which can be very different from each other due to the height difference; see ALMA Partnership et al. 2015a for details), has been removed from each dataset (the antenna position errors are generally small enough that they only cause linear phase drift on timescales of tens of minutes or more). After this, we averaged the data points for 10 s to take out phase errors due to thermal noise. With this 10 s time averaging, and assume the source flux density is 1 Jy and the system temperature is a typical value for each ALMA Band (Remijan et al. 2015), root mean square (rms) phase errors due to thermal noise are calculated as 3.4, 2.0, 2.4, and 4.5 μm for Bands 3, 6, 7, and 8, respectively. In our observations, the minimum source flux densities are 1.7, 1.1, 1.2, and 3.7 Jy for Bands 3, 6, 7, and 8, respectively, so that the maximum rms phase errors can be calculated as 2.0, 1.8, 2.0, and 1.2 μm for Bands 3, 6, 7, and 8, respectively. The smallest measured phase fluctuation at very short baseline lengths of about 15 m before the WVR phase correction, but after the 10 s averaging, is about 6 μm (Matsushita et al. 2012), which is larger than the upper limit of the phase error. We can therefore conclude that we successfully suppressed the effect of instrumental noise in our data with 10 s averaging.

[11]Longer measurement time of 90 minutes has also been tested; see Sect. 3.2.2.

[12]WVR phase correction method is to estimate the amount of water vapor in front of each antenna using the 183 GHz WVR (Nikolic et al. 2013), calculate the excess path length and phase difference between antennas, then correct the phase fluctuation caused by water vapor (Wiedner et al. 2001; Nikolic et al. 2013).

We then calculated the rms phase fluctuation for each baseline. For the unit of phase, we express in path length[13]. This allows us to directly compare the results from various frequencies in the same unit without any frequency dependence, and is often referred to as excess path length.

3. Results and Discussion

3.1. Improvement Factor of the WVR Phase Correction

WVR phase correction often improves the data quality (Matsushita et al. 2012, 2014; Nikolic et al. 2013; ALMA Partnership et al. 2015a), but there is no statistical study how much it improves for short to long baselines. In this subsection, we present the statistical study results for this method.

Fig. 1(a) shows the rms excess path length before (filled symbols) and after (open symbols) the WVR phase correction for the data with baseline length longer than 1 km (data for baseline length $>$ 1 km in eahc data set have been averaged into one data point). It is obvious that the WVR phase correction reduces all the rms excess path lengths to less than 1000 μm.

The improvement factor of the WVR phase correction method has been calculated as the ratio of the rms excess path length for each baseline without the WVR phase correction to that with the correction. Higher values mean that the WVR phase correction works better (improved more) than cases with lower values (less improvement). Values of less than unity means that the WVR phase correction made the phase fluctuation worse than the original data. Calculated values are averaged over all baselines, and plotted as a function of PWV (Fig. 1b). In addition, we plotted the data divided into baseline lengths shorter and longer than 1 km (Fig. 1c). For the former, we used data from all campaigns; for the latter, we use only data from the 2014 campaign, since the older data contain very few long baselines.

The mean improvement factor over all PWV conditions is 2.1 ± 0.7. This result is consistent with what is reported previously (Matsushita et al. 2012; ALMA Partnership et al. 2015a), but this is the first statistical result. However, from Fig. 1(b), it is obvious that the improvement factor is often larger when PWV is larger than 1 mm, with a mean improvement factor of 2.4 ± 0.7. In the case of PWV $<$ 1 mm, however, the ratio is 1.7 ± 0.4. Thus it is clear that although the WVR phase correction in most cases provides an improvement in the amount of phase fluctuation, the amount of improvement can be significantly larger for PWV $>$ 1 mm. This result can be explained because at low PWV, the difference in the amount of water vapor along the lines of sight of two antennas is small compared to the thermal noise of the WVRs of ~ 0.1 K rms (which corresponds to about a few tens micron rms; Nikolic et al. 2013). In addition, scatter of the data points is also different between low and high PWV cases, which is obvious in Fig. 1(b) and also from the error values of

[13] $\Phi = \frac{\theta}{360^\circ} \times \frac{c}{\nu}$, where Φ and θ are phase in path length and in degrees, respectively, c is the speed of light, and ν is the observation frequency.

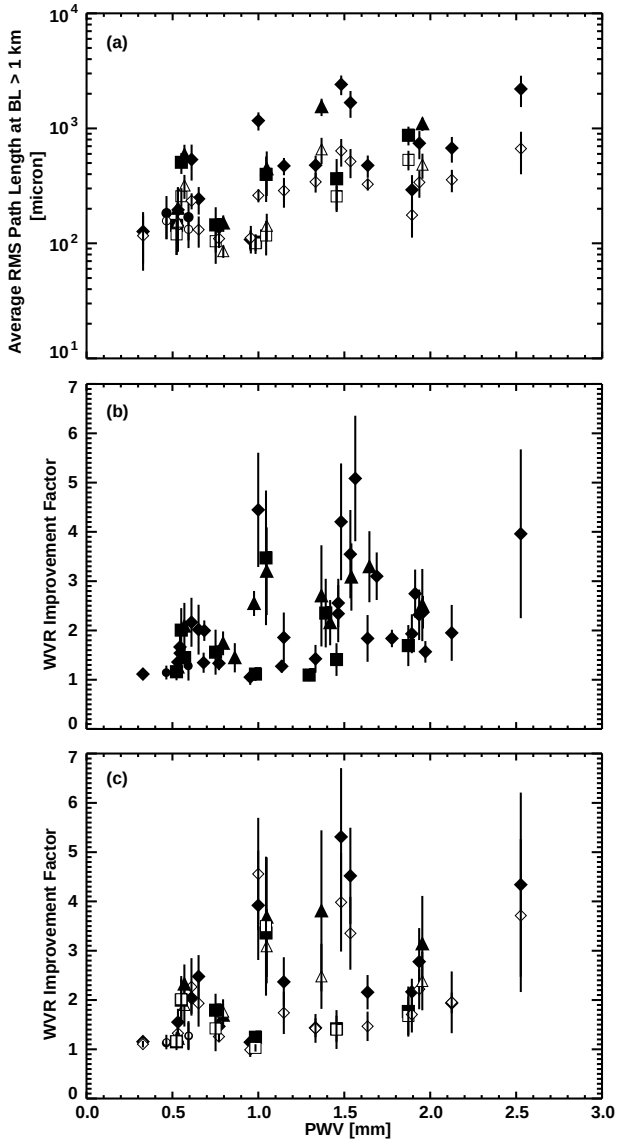

Fig. 1.— (a) Averaged rms excess path length at baseline lengths longer than 1 km. This plot only uses the 2014 data, since only the 2014 data have statistically significant data points at baselines longer than 1 km. Symbols are differentiated with the frequency bands; diamond, triangle, square, and circle symbols indicate the data taken with Bands 3, 6, 7, and 8, respectively. Filled and open symbols are before and after the WVR phase correction, respectively. (b) Improvement factor of the WVR phase correction (ratio of the rms excess path length without WVR phase correction to that with the correction) as a function of PWV. Each data point is averaged over all baselines. This plot uses all the 2012 – 2014 data. (c) Data points have been separated for the one averaged over the baseline length shorter (filled) or longer (open) than 1 km. The open symbol data points are calculated from the data shown in (a).

about twice difference (± 0.7 vs ± 0.4) as mentioned above. This means that not all the data show significant improvement in phase fluctuation in the case of PWV > 1 mm after the WVR phase correction.

Fig. 1(c) shows that the improvement factor for the baseline length shorter than 1 km is 2.3 ± 0.9, and that for the baseline length longer than 1 km is 2.0 ± 0.7. The longer baseline data tend to have lower improvement factor than the shorter ones, although the difference is statistically not significant.

In both plots, different frequency bands are plotted with different symbols, but we find no significant difference in the improvement factor as a function of frequency band.

3.2. Spatial Structure Function of Phase Fluctuation

In this subsection, we first define the spatial structure function (SSF) of phase (Sect. 3.2.1), and derive the SSF slopes (Sect. 3.2.2) and constants (Sect. 3.2.4) for all the past long baseline single source stare data. Statistical result for the slopes is compared with the previously published studies (Sect. 3.2.2). We then estimate the rms phase fluctuation for a 10 km baseline, and derive a weak correlation with PWV (Sect. 3.2.4). After WVR phase correction, there is a significant residual phase fluctuation, suggesting that there may be other constituents than water vapor that cause the phase fluctuation exist in the atmosphere; we discuss the possibilities for liquid water, ice, and dry components, and also any instrumental causes (Sect. 3.2.5).

3.2.1. Definition of Spatial Structure Function

The SSF of phase is defined as

$$D_\theta(d) = < \{\theta(x) - \theta(x-d)\}^2 >, \tag{1}$$

where $\theta(x)$ and $\theta(x-d)$ are phases at positions x and $x-d$, and the angle brackets mean an ensemble average (Tatarskii 1961; Thompson et al. 2001). Since $\theta(x) - \theta(x-d)$ is an interferometer phase with a baseline length d, $\sqrt{D_\theta(d)}$ is approximated to the rms phase fluctuation of a baseline over the entire observation time. SSF plots in this paper have therefore been made by calculating the rms phase for each projected baseline in the direction of a target source using tens of minutes of observation time, and plotted as a function of baseline length.

Slopes for rms phase fluctuation are well studied theoretically, and in the case of 3-dimensional (3-D) Kolmogolov turbulence of the Earth's atmosphere, it is expected to have a slope of 0.83; for the 2-D turbulence case, the slope is expected to be 0.33. In the case of no correlation in the atmospheric turbulence between two antennas, the slope is expected to be zero (Thompson et al. 2001).

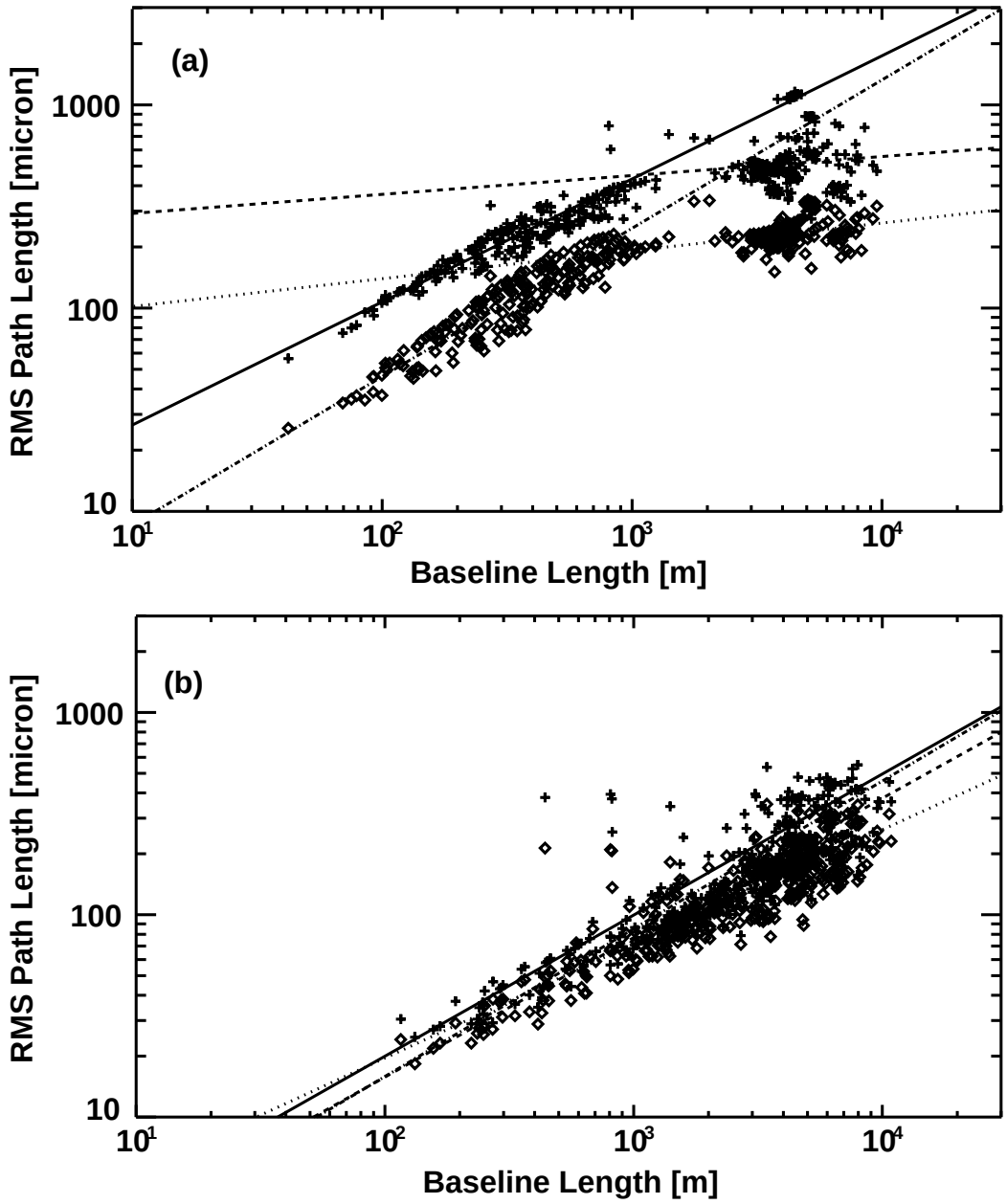

Fig. 2.— Two representative plots of the spatial structure function (SSF) with (open diamond) and without (cross) WVR phase correction. Solid and dashed lines are the fitting results of slopes using baselines shorter than 500 m and longer than 1 km, respectively. (a) Example of SSF with a clear turn-over. The data file for this plot is "uid__A002_X8bd3e8_Xa59" in Table 5. (b) Example of SSF without any clear turn-over. The data file for this plot is "uid__A002_X8e1004_Xf04" in Table 5.

Fig. 2 shows two example plots of SSFs we obtained using the ALMA data. In these plots, both the WVR phase corrected and uncorrected SSFs are displayed. As mentioned above, phase is converted into the unit of path length. Fig. 2(a) displays a typical SSF plot; there is a clear turn-over in the SSF at baseline lengths of $\sim$ 1 km in both plots with and without the WVR phase correction. Shorter baselines, before the turn-over, show a steeper slope, while longer baselines show a shallow or almost flat slope. In general, for the 'typical' data sets, only one turn-over is evident with the current data analysis method, and is usually observed between baseline lengths of several hundred meters to $\sim$ 1 km. Fig. 2(b), on the other hand, exhibits no clear turn-over; phase fluctuation increases constantly even at long baselines. Such a constant slope SSF is not common, but is sometimes observed in the data (see Sect. 3.2.2 for statistics). Note that these no turn-over data generally have a much lower excess path length value compared to the 'typical' data at particular baseline lengths (especially at shorter baselines), which can be seen in Fig. 2. This means that the SSF with a constant slope is inherently more stable than that with a turn-over (see also the end of Sect. 3.2.2).

The baseline length of the turn-over roughly corresponds to the scale height of the three-dimensional atmospheric turbulence (Treuhaft & Lanyi 1987; Lay 1997). Our results suggest that the scale height of the water vapor constituent at the ALMA site is about 1 km in most cases, which is a typical value of the turn-over baseline length measured with astronomical radio arrays (e.g., Carilli & Holdaway 1999). It is highly possible that the main turbulent constituent at the ALMA site is water vapor, which is consistent with the improvement of phase fluctuation by the WVR phase correction in most cases (Sect. 3.1). On the other hand, no turn-over means that the scale height of the turbulent constituent is higher than 10 km. This scale height is much higher than that of water vapor, suggesting that the turbulent constituent for the SSF with no turn-over is caused by some other constituent (see Sect. 3.2.5 for further discussion).

3.2.2. Slopes for the Spatial Structure Functions

We first fitted the slopes for the data points with baseline lengths shorter than 500 m and longer than 1 km for each SSF plot, namely shorter and longer than the turn-overs in the plots. The fitting function is expressed as

$$\log_{10}(\Delta L) = a \times \log_{10}(d) + b, \tag{2}$$

where ΔL is the rms excess path length in micron, d is the baseline length in meter, and a and b are the slope, namely the structure exponent, and the structure constant, respectively. Examples of the fitting are shown in Fig. 2, and the fitted slopes as a function of PWV are plotted in Fig. 3; (a) is for the shorter baseline slopes, and (b) for the longer baseline slopes.

In Fig. 3(a), there is no significant trend either as a function of PWV, frequency, or the effect of the WVR phase correction. The fitted slopes before and after the WVR phase correction with averaging all the data, and that with PWV lower and higher than 1 mm are shown in the top

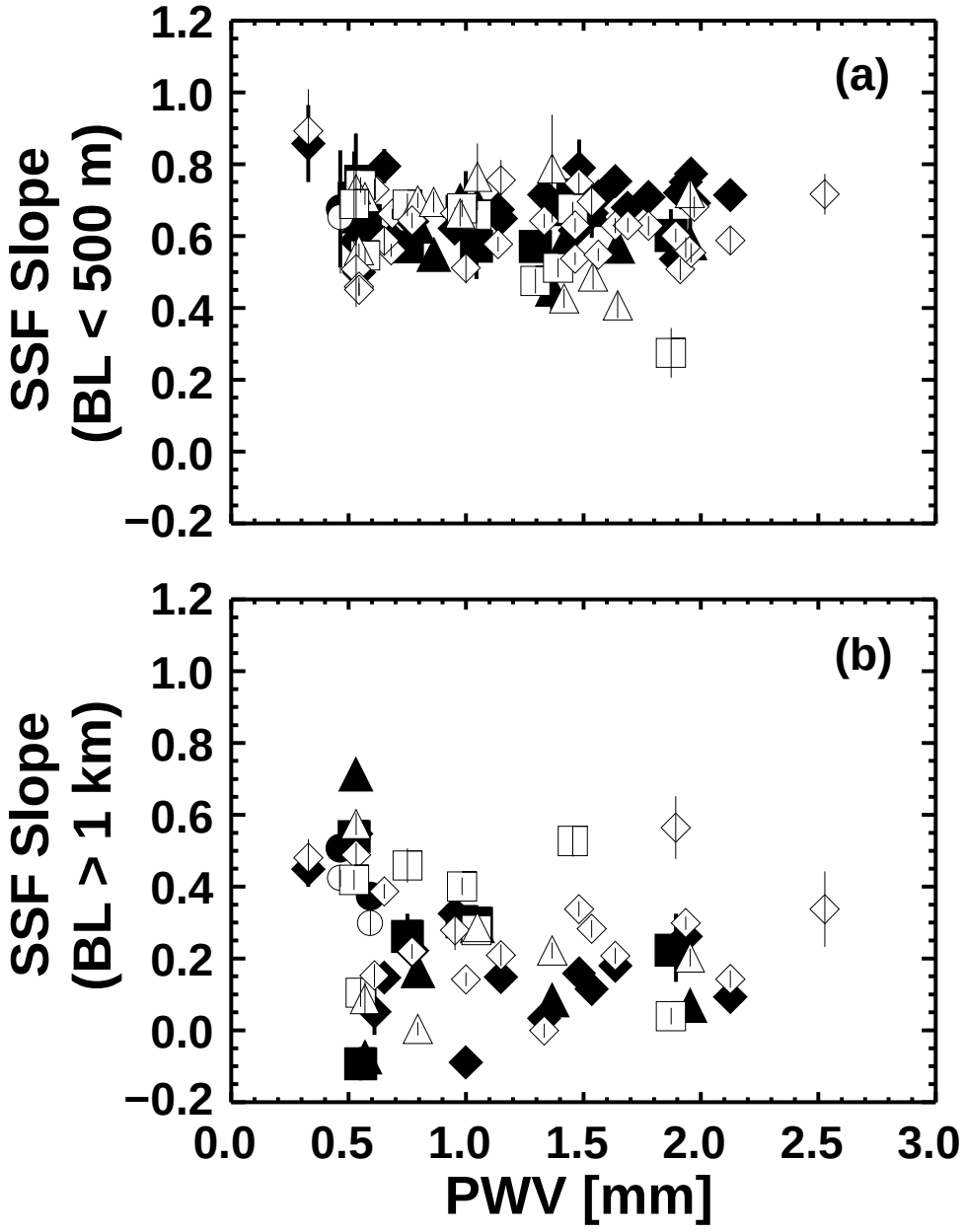

Fig. 3.— Fitted slopes of the spatial structure functions (SSFs) as a function of PWV. (a) Slopes for the data points in each SSF with the baseline lengths shorter than 500 m, and (b) longer than 1 km. Symbols are differentiated with the frequency bands; diamond, triangle, square, and circle symbols indicate the data taken with Bands 3, 6, 7, and 8, respectively. Filled symbols are the data before the WVR phase correction, and open symbols after. Note that (a) includes the 2012 – 2014 data, but (b) only includes the 2014 data, for the reason same as in Sect. 3.1.

row of Table 1. All those values are around 0.6, indicating that the WVR phase correction or the amount of water vapor in the atmosphere does not change the shorter baseline slopes of SSFs. The average slope without the WVR phase correction of 0.65 ± 0.06 is consistent with the 50% quartile slope for the 3-year (1996 July – 1999 March) statistical data using the site testing 11.2 GHz radio seeing monitor of 0.63 (Butler et al. 2001). This indicates that the data we took are typical phase fluctuation characteristics at the ALMA site.

Fig. 3(b) clearly shows that the slopes at longer baselines (baseline length > 1 km) are shallower than the shorter baselines (baseline length < 500 m; Fig. 3a) in most cases. Similar to the above, the fitted slopes are shown in the bottom row of Table 1. The average slopes are 0.22 ± 0.15 and 0.29 ± 0.13 for the data before and after the WVR phase correction, respectively. These values are significantly smaller than those for the baseline length shorter than 500 m, indicating that most of the data have a turn-over at a baseline length between 500 m and 1 km.

For almost all the cases, the slopes for shorter baselines are in the middle of theoretical 3-D and 2-D Kolmogorov turbulence, which are 0.83 and 0.33, respectively. This suggests the existence of undeveloped turbulence or multi-layer turbulence with different heights in the atmosphere. The slopes for longer baselines (slopes after the turn-over), on the other hand, exhibit the values between the 2-D Kolmogorov turbulence (slope = 0.33) and no correlation between two antennas (slope = 0) in most cases.

Our result is very similar to the result from the statistical study of the SSF slope at the VLA site; the slope of 0.59 at short (< 1 km) baselines, and 0.3 at longer baselines (Sramek 1990). On the other hand, later SSF study with long measurement time of 90 minutes (Carilli & Holdaway 1999) exhibits two clear turn-overs, one from the 3-D Kolmogorov turbulence (slope = 0.83) to the 2-D one (slope = 0.33), and the other from the 2-D one to the no-correlation regime (slope = 0). SSFs with two turn-overs has never been obtained in the statistical study by Sramek (1990), suggesting that SSFs with two turn-overs are statistically rare, the coverage of the array configuration was not wide enough to investigate the full range of the atmospheric turbulence, or the measurement time was not long enough. Note that we took one 90 minutes long data (see "uid__A002_X8e1004_Xfe5" in Table 5), but this data set did not show two turn-overs as Carilli & Holdaway (1999), but showed similar feature as the 30 minutes long data taken in the same day.

For PWV < 1 mm, the average of the slope at longer baselines is much smaller than that for the shorter baselines, but the scatter of the slope is large (Table 1), and the highest values of the

Table 1. Fitted slopes of the spatial structure functions (SSFs).

	Without WVR phase correction			With WVR phase correction		
Baseline Length	All	PWV < 1 mm	PWV > 1 mm	All	PWV < 1 mm	PWV > 1 mm
< 500 m	0.65 ± 0.06	0.65 ± 0.06	0.66 ± 0.06	0.62 ± 0.09	0.64 ± 0.08	0.60 ± 0.09
> 1 km	0.22 ± 0.15	0.27 ± 0.20	0.17 ± 0.07	0.29 ± 0.13	0.31 ± 0.15	0.26 ± 0.11

slope are almost the same as that of the shorter baselines. This means that there are some cases that do not have any turn-over; an example is shown in Fig. 2(b). As mentioned in Sect. 3.1, at this low PWV range, the improvement factor of the WVR phase correction is not high, suggesting that the phase fluctuation is not due to water vapor but caused by another constituent, the same conclusion as above (Sect. 3.2.1).

For PWV > 1 mm and without the WVR phase correction, the slopes are always small (small values with small scatter; Table 1), but after the WVR phase correction, both the slope and the scatter are large. This, together with the improvement factor of the WVR phase correction mentioned above (Sect. 3.1), indicates that in many of the cases the slopes turn to be steeper after the WVR phase correction for the longer (> 1 km) baselines. For some cases, the slopes become similar to the slope at shorter (< 500 m) baselines, namely SSF being similar to the one with no turn-over, suggesting that the WVR phase correction took out all the phase fluctuation caused by water vapor, and that caused by another constituent remains. This means that if we can completely remove the phase fluctuation due to water vapor in the atmosphere, a large-scale turbulent component that covers the longest baseline lengths is revealed. This also means that phase fluctuation due to the large-scale turbulent component is inherently smaller than that due to water vapor.

3.2.3. Constants for the Spatial Structure Functions

Figs. 4(a) and (b) display the derived structure constants b in Eq. 2 as a function of PWV for baseline lengths shorter than 500 m and longer than 1 km, respectively. For both cases, there is a weak correlation between the structure constants and PWV for both before and after the WVR phase correction (the solid and dashed lines, respectively in Fig. 4).

With the average slope a in Table 1 and the fitted results of the structure constant b in Fig. 4, it is possible to estimate the rms excess path length on any baseline length for the current ALMA (i.e., baseline length up to 15 km). Note that the scatter is large so that this estimation is useful only to tell the tendency of the phase fluctuation.

3.2.4. Phase Fluctuation on 10 km Baselines

To understand quantitatively how much phase fluctuation exists at long baselines, we calculate the rms excess path length for the baseline length at 10 km. Although the averaged slope at baseline lengths longer than 1 km is around $0.2 - 0.3$ (see Sect. 3.2.2), the slope at baseline lengths longer than 10 km is expected to be close to zero, namely no increase of the rms excess path length (Carilli & Holdaway 1999). Therefore it is expected that the rms excess path length at 10 km is roughly equal to the rms excess path length longer than 10 km. Here, we estimate the rms excess path length at 10 km using the fitting results derived in the previous subsection. This information will

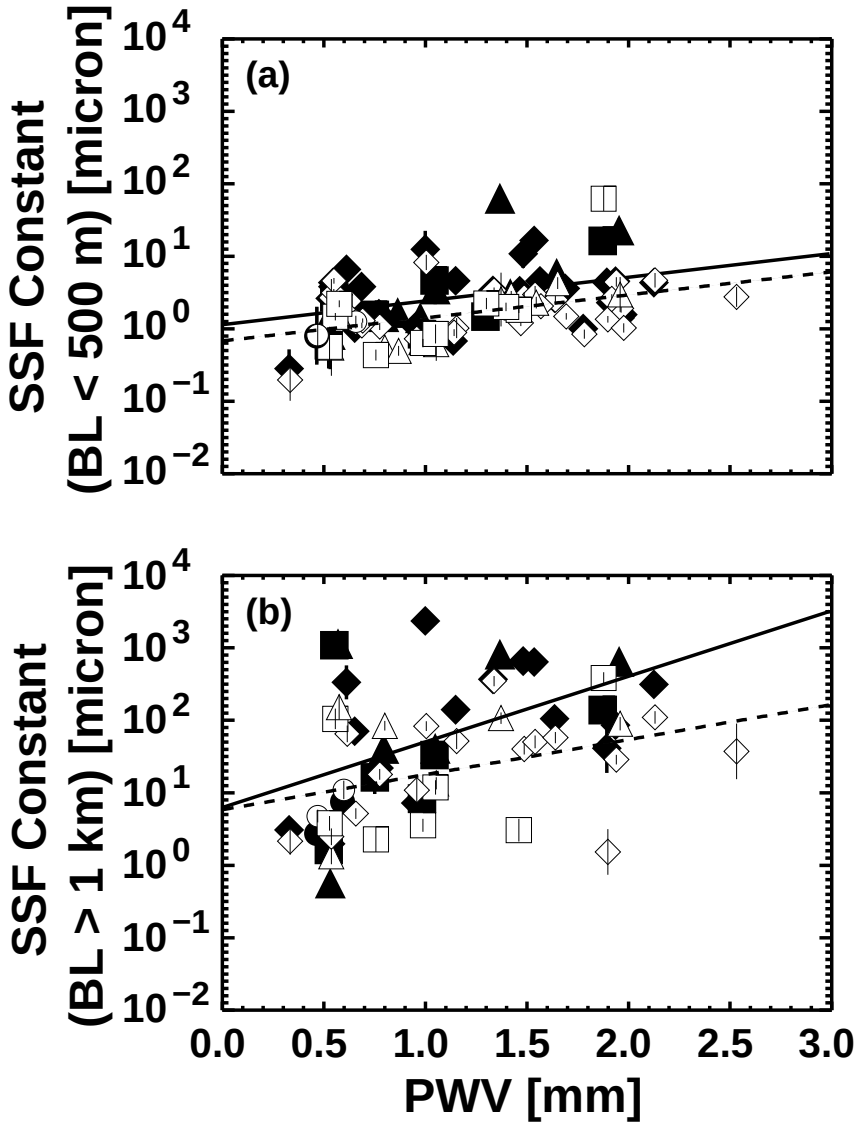

Fig. 4.— Fitted structure constants of SSFs as a function of PWV. Symbols and their colors are the same as in Fig. 3. (a) Structure constants for the data points in each SSF with the baseline lengths shorter than 500 m. Solid [$b_{raw} = (0.3 \pm 0.1) \times \mathrm{PWV} + (0.1 \pm 0.1)$] and dashed [$b_{wvr} = (0.3 \pm 0.1) \times \mathrm{PWV} - (0.2 \pm 0.1)$] lines are the fitting results for the data before and after the WVR phase correction, respectively. (b) Structure constants for the data points in each SSF with the baseline lengths longer than 1 km. Solid [$b_{raw} = (0.9 \pm 0.3) \times \mathrm{PWV} + (0.8 \pm 0.4)$] and dashed [$b_{wvr} = (0.5 \pm 0.2) \times \mathrm{PWV} + (0.8 \pm 0.3)$] lines are the fitting results for the data before and after the WVR phase correction, respectively.

be useful for high frequency observations, or future extended-ALMA (Kameno et al. 2013), which is to extend the maximum baseline lengths longer than the current ALMA (> 16 km), or Very Long Baseline Interferometry (VLBI) observations, which will have much longer baseline lengths (> 100 km).

Using Eq. (2) to fit the data with baseline lengths longer than 1 km, we estimated the rms excess path length at a baseline length of 10 km. Fig. 5 displays the estimated rms excess path length at a baseline length of 10 km as a function of PWV for both before and after the WVR phase correction. As expected from a weak correlation between the structure constant b and PWV, both data set show a weak correlation with PWV (see the solid and dashed lines for the fitting results); lower PWV conditions tend to have smaller rms excess path length, and opposite for higher PWV conditions. This is understandable since a larger amount of water vapor in the atmosphere provides a greater possibility for larger phase fluctuations caused by increased differences in the water vapor content over the array. On the other hand, the scatter is large, almost an order of magnitude at a given PWV ranges, which makes the correlation weak. This indicates that the phase fluctuation cannot only be the fucntion of the total water vapor content in the atmosphere.

For almost all the data, there is a significant rms excess path length after the WVR phase correction, with a mean value of 206 μm even at PWV < 1 mm. This result indicates that even after the WVR phase correction under good weather conditions, peak-to-peak phase fluctuation reaches around 2π or more at the high frequency bands (i.e., Bands 9 & 10; $600 - 1000$ GHz or $300 - 500$ μm) over ~ 10 minute timescales. This phase fluctuation blurs the final synthesized image, with the blurring size around twice the synthesized beam size or more, significantly affects the imaging quality, if we calibrate the phase at the same frequency. One way to mitigate the 2π ambiguity problem in the phase calibration is to use a calibrator phase at lower frequency and to apply the solutions to the target at higher frequency, i.e., band-to-band phase calibration and/or using the fast switching phase correction method. The former phase calibration technique has another advantage in ALMA; because the array sensitivity is higher at lower frequencies, fainter phase calibrators are available at lower frequency even though the thermal noise in phase is scaled up with the frequency ratio. This leads another advantage of the availability of the phase calibrator; it becomes easier to find a closer phase calibrator to a science target source. The fast switching phase correction is further discussed in Sect. 3.4.

3.2.5. Why Does the WVR Phase Correction Not Take Out All the Phase Fluctuation?

In most cases, the main difference between SSFs with and without the WVR phase correction is the reduction in the absolute rms phase (rms path length) values (Fig. 1a), whereas the overall shapes and slopes do not change significantly with the WVR phase correction (Fig. 2a) and are only weakly correlated with PWV (Fig. 5). The WVR phase correction improves the rms path lengths by a factor of 2 on average (Sect. 3.1). If the WVR phase correction takes out all the phase fluctuation, the resultant spatial structure function should exhibit an almost flat feature; since the

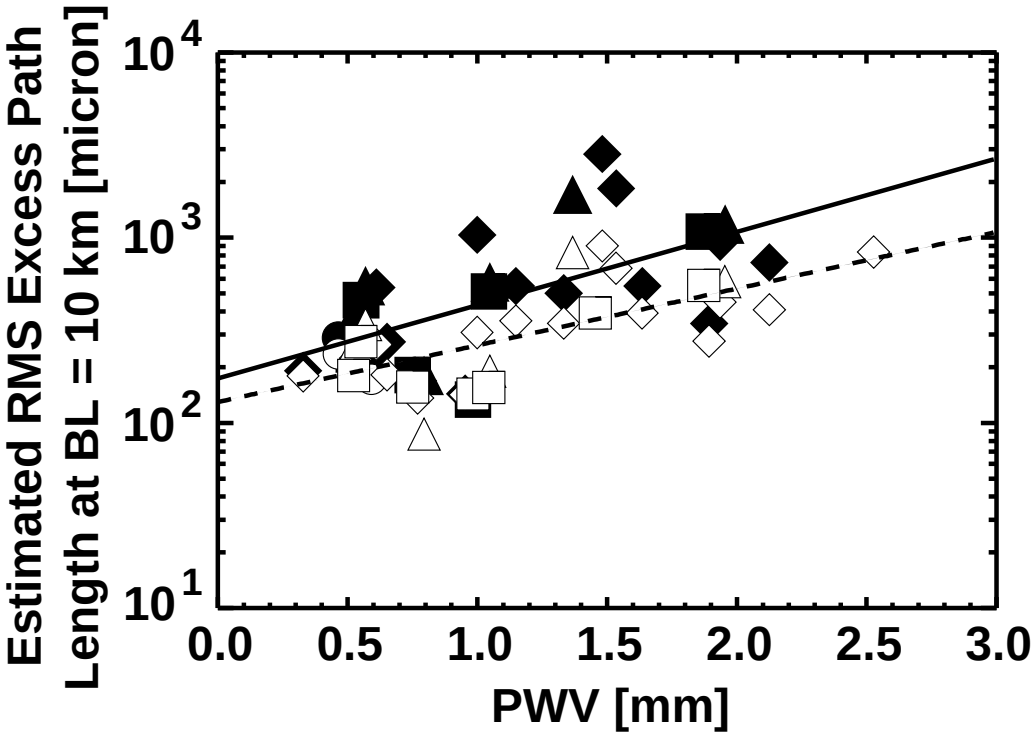

Fig. 5.— Estimated rms excess path length of each data set taken in 2014 at a baseline length of 10 km using the fitted results mentioned in Sect. 3.2.2, which roughly represents the rms excess path length even longer than 10 km. Solid and dashed lines are the fitting results for the estimated rms excess path length before and after the WVR phase correction, respectively. Symbols and their colors are the same as in Fig. 3.

WVR phase correction is applied to the data every 1 second, if the wind blows along a baseline with a velocity of 10 m s^{-1} and assuming a frozen phase screen, then the phase at the baselines longer than 10 m should show random phase that corresponds to the thermal noise of the WVRs. We have never observed such a SSF in the last 5 years of the long baseline campaigns (see also Matsushita et al. 2012, 2014, 2016). The overall similarity between the SSFs with and without the WVR phase correction suggests that the origin of the phase fluctuation is not only due to the water vapor but also other turbulent constituents. Furthermore, SSFs without any turn-over also suggests the existence of other turbulent constituents with scale height larger than the longest baseline length of $\sim$ 10 km, as mentioned above (Sect. 3.2.1, 3.2.2).

The cause of this remaining phase fluctuation is still unclear: Turbulent eddies excited by wind blowing over the mountains can cause additional phase fluctuation. Indeed, some raw data show this effect, especially data from antennas near mountains, but the phase fluctuation caused by this effect can be cleanly removed by the WVR phase correction (Asaki et al. 2016). Therefore this effect cannot be the cause of the remaining phase fluctuation. The remaining phase fluctuation can also be due to wind speed or its direction parallel or perpendicular to baseline directions. This will be discussed in the forthcoming paper (Maud et al., in prep.), so that we do not discuss here. Liquid water (fog or clouds) in the atmosphere absorbs the amplitude of electromagnetic waves significantly (Ray 1972; Liebe 1989; Liebe et al. 1991) at continuum level. This changes the line profile of the water vapor in the atmosphere, so that the WVR phase correction, which uses the liquid water-free line profile model, will no longer be appropriate (Matsushita et al. 2000; Matsushita & Matsuo 2003). Therefore if liquid water dominates the atmosphere, then the rms phase after WVR phase correction will not improve or will even be worse. Since we are looking for the cause of the remaining phase fluctuation *after* successful WVR phase correction, liquid water cannot be the cause. Water ice in the atmosphere, which is not detected by the WVR, can induce similar phase fluctuations to water vapor (Hufford 1991; Liebe et al. 1993). Density fluctuations of a dry component (i.e., N_2 and O_2) in the atmosphere could also be the cause of phase fluctuations (Nikolic et al. 2013). Both water ice and a dry component have a high scale height of around 10 km or more, so that the SSFs with no turn-over can be explained by these constituents. Although it is not clear whether the water ice always exists in the atmosphere, and the density fluctuations are still not confirmed observationally, those two atmospheric components could potentially be the causes.

Instrumentation problems could also be a possibility; since the SSF is baseline-based, instruments that could cause baseline-based problems needed to be considered. The correlator is one of the baseline-base instruments, but it is very unlikely that this could produce larger phase fluctuation selectively at longer baselines all the time, because the correlation process after analog-to-digital conversion of the received signals at each antenna is highly digitized. The Line Length Corrector (LLC; round-trip phase corrector) is an instrument that can create phase noise as a function of baseline length; noise in this instrumental component causes antenna-based phase noise, but the atmospheric phase fluctuation is baseline-based, so that the relative effect of LLC phase noise is

larger for shorter baselines and smaller for longer baselines, namely it appears as baseline-based. However, the variation of the LLC in each antenna is always monitored, and the timescale of the variation is much longer than the observed phase fluctuation. This indicates that the LLCs are unlikely to cause the phase fluctuation.

3.3. Coherence Time

The temporal coherence function is defined as

$$C(T) = \left| \frac{1}{T} \int_0^T \exp\{-i\theta(t)\} dt \right|, \tag{3}$$

where $\theta(t)$ is phase at a time t and T is an arbitrary integration time (Thompson et al. 2001). This equation is namely a vector averaging of phase in the time domain. A coherence of unity means no loss in coherence (i.e., amplitude) due to the phase fluctuation, and that of zero means no coherence at all due to huge phase fluctuation. Coherence time is a maximum T at which the coherence is not smaller than a certain critical value; since phase fluctuation increases as time passes from a certain time, coherence decreases.

Coherence time is closely connected with an integration time for one data point for radio arrays; if one can tolerate a certain coherence loss, one could define the integration time based on the coherence time. This is also true for the calibration time interval; for a typical interferometric observation, a phase calibrator will be observed at certain time intervals, and if one can tolerate a certain coherence loss, one could define the calibration time interval based on the coherence time.

In addition, this is also relevant for the integration time of VLBI; for detecting interferometric signals (i.e., fringes) with VLBI, it is important to have high signal-to-noise ratio within one data point, since it is needed to search the signal in the ranges of delay and delay rate due to uncertainty in the antenna locations (i.e., fringe search). On the other hand, since the atmosphere will affect the VLBI phase stability significantly, we should be careful in selecting the integration time for VLBI observations, especially in mm/submm wave. The coherence time is a good indicator of ideal integration time for the signal detection with VLBI. This information will be useful for VLBI using single dish telescopes close to ALMA, namely APEX and ASTE. Furthermore, VLBI using ALMA (ALMA Phase-Up Project), which is to add signals from the ALMA antennas in phase in real time to produce a single VLBI "station", or so-called phased array, needs stable atmospheric phase to obtain high efficiency in adding in phase. The coherence time is also good to find out the ideal data adding time length in real time to have high efficiency for phase-up.

Since the phase fluctuation depends on the baseline length, but the slope will be significantly shallower at baseline lengths longer than 1 km (see Sect. 3.2), we take a median value of the coherence time derived from the data at baseline lengths longer than 1 km. Here, we calculate the coherence time that degrades the coherence to 0.9 (i.e., coherence loss of 10%). The calculation results are shown in Fig. 6 as a function of PWV. Each calculation stops at the time range of 400

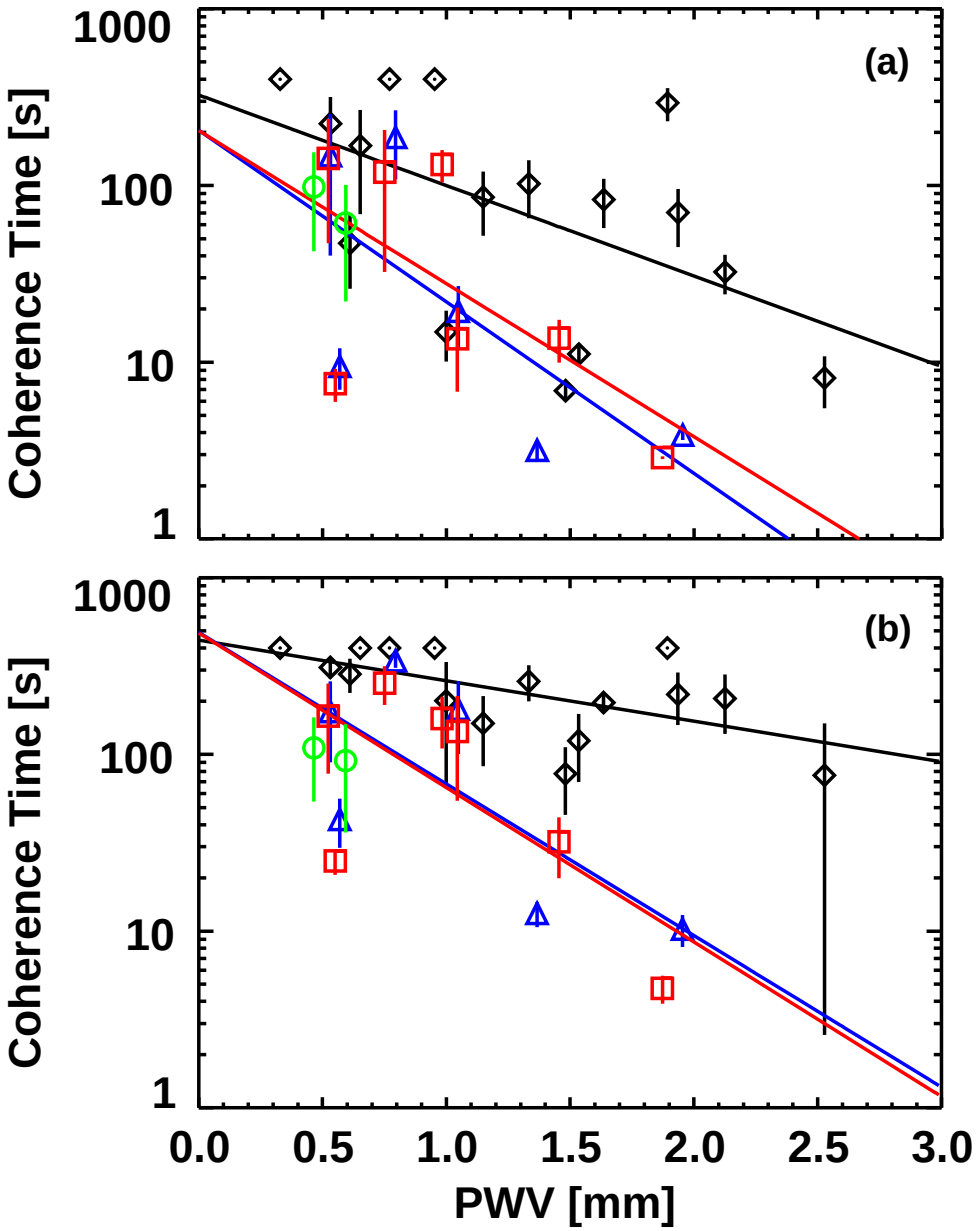

Fig. 6.— Coherence time that lead to a degraded coherence of 0.9 (i.e., coherence loss of 10%) as a function of PWV. Each data point in the plot is a median of the coherence time of each baseline with its length longer than 1 km in each data set. (a) The data before the WVR phase correction, and (b) after. Colors for the symbols and the fitted lines are different in bands; black, blue, red, and green are for Bands 3, 6, 7, and 8 data, respectively. There is no fitted line for Band 8, since there are not enough data points. Symbols are the same as in Fig. 3.

s, since ALMA will not calibrate phase on such long timescales. So the data points located at 400 s means that these did not reach the coherence loss of 10% even after 400 s. It is obvious that the data after the WVR phase correction have longer coherence time than that without. The average of the coherence time after the WVR phase correction is 184 s, about twice longer than that without (101 s). This indicates that the WVR phase correction improves the coherence time by about twice or more (since our calculation stops at 400 s, the coherence time is underestimated, especially for the WVR phase corrected data with the time longer than 400 s). The WVR phase correction is therefore useful for extending integration or calibration time interval.

In terms of overall PWV dependency of coherence time, there is a weak trend for lower PWV to give rise to longer coherence time. This can be understood as more water vapor in the atmosphere, causing more phase fluctuation and therefore larger coherence loss. However, the scatter is very large, more than an order of magnitude of coherence time at a certain PWV, suggesting that phase fluctuation is not a simple function of the amount of water vapor in the atmosphere. This result is the same as Sect. 3.2.4, since we are showing the same data with different expressions.

The trend appears to depend on frequency band; Band 3 has larger scatter with less dependence on PWV, but Bands 6 and 7 have smaller scatter with tight dependence on PWV (see the fitted lines in Fig. 6). This can be explained as follows; observations at Band 3 can be carried out under a wider range of PWV, but for Bands 6 and 7, the observation conditions are limited to better weather and the phase fluctuation quickly gets worse as weather conditions get worse.

3.4. Fast Switching Simulation

The fast switching phase correction method is to switch between the science target source and a nearby calibrator quickly (faster than a time scale on which the phases of both the target and the calibrator differ from each other), and calibrate the phase fluctuation (Carilli & Holdaway 1999; Morita et al. 2000; Asaki et al. 2014, 2016). The importance of this method is now better understood than it was in the past. This is because no matter what causes the phase fluctuation, this method can improve the phase stability to cancel out not only the atmospheric phase fluctuations, but also the instrumental phase errors, such as a frequency standard, which the WVR phase correction cannot remove. Compared with the WVR phase correction method, which takes out shorter time scale phase fluctuation (order of $\sim$ 1 second to $\sim$ 1 minute scale), the fast switching phase correction method takes out longer time scale phase fluctuation (tens of second or longer). Combining those two methods, it is expected to take out a significant amount of phase fluctuation, and improve the data quality significantly.

Using the single source stare data taken in 2014, it is possible to simulate the fast switching phase calibration by separating the data into "target", "calibrator", and "antenna slew time" components, and making an image for the "target" (calibrated using the "calibrator" data). Comparing the peak flux of the calibrated "target" image with that of the self-calibrated image, namely

calculating the coherence of the data, it is possible to estimate the effect of the fast switching phase correction method quantitatively by changing the cycle time (i.e., time for "calibrator" → "target" → "calibrator," including the antenna slew time between the calibrator and the target). This simulation is an idealized case, since the "target" and the "calibrator" do have the same atmospheric phase fluctuation in this simulation, which is not true for the real case; it depends on the separation between the "target" and the "calibrator" (Asaki et al. 1996, 1998). This simulation is nonetheless useful for testing the effect of cycle time.

In this paper, we simulated three cycle times: 28 s, 48 s, and 68 s (see Table 2). In all cases, we used an integration time for the target of three times the integration time for the calibrator and a slew time of 4 s, which are reasonable for the actual observational setup. Note that the simulated observations always start from and end with the phase calibrator scan.

We then calibrated the "target" data with the "calibrator" data, and imaged the "target" using the CASA software and a standard interferometric imaging procedure. We also produced the self-calibrated image for the "target", and we used this image as a reference to compare the peak flux of the simulated image. The coherence of the fast switching method is estimated by calculating the ratio of the peak flux densities between the fast switching simulation image and the self-calibrated one.

The results of the simulation — coherence as a function of cycle time for various frequency bands (Bands 3, 6, 7, and 8) are shown in Fig. 7. We also overplotted linear fitting results of coherence as a function of cycle time as solid lines. It is obvious that longer cycle time lead to lower coherence. In addition, the decrease of coherence as a function of cycle time appears almost linear. This indicates that fast switching with shorter cycle times could lead to higher quality images. This is true irrespective of frequency band and weather conditions. On the other hand, since we did not consider the separation between the "target" and the "calibrator" as mentioned above, this linear increase of the coherence as a shorter cycle time will be non-linear or even stop at some point in the case of a real observation, due to the different atmospheric conditions toward these two sources. The point at which this happens may highly depends on the separation between the "target" and the "calibrator," and the actual observational testing of the fast switching phase correction method

Table 2. Time distribution of the cycle time for the fast switching simulation.

Cycle Time [s]	Target [s]	Calibrator [s]	Antenna Slew [s]
28	15	5	4
48	30	10	4
68	45	15	4

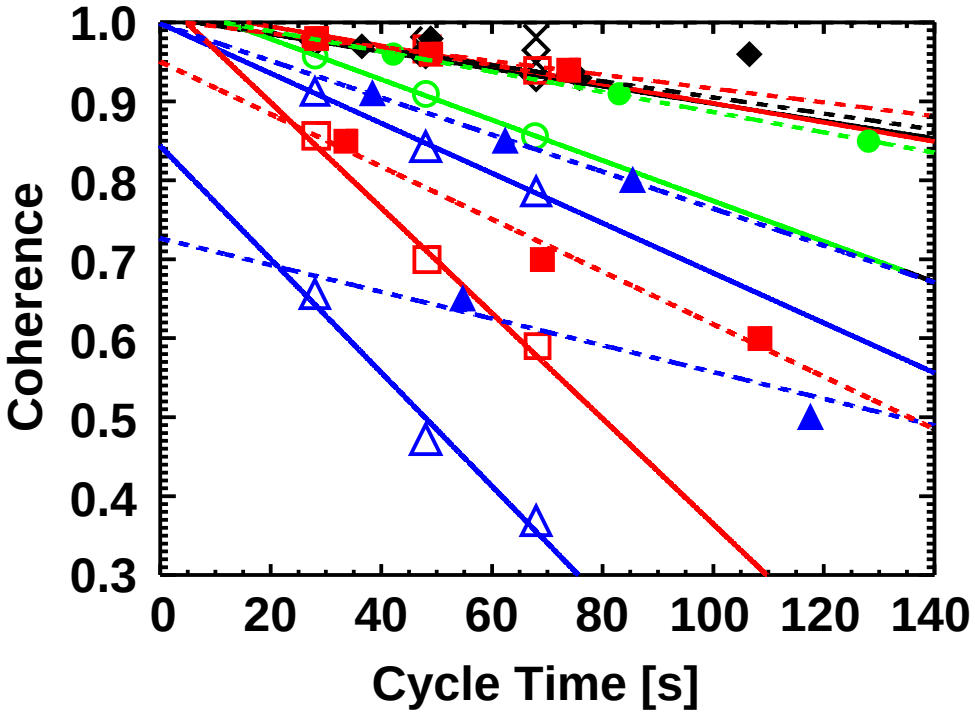

Fig. 7.— Plot of coherence as a function of fast switching cycle time for the simulated fast switching method using the single source stare data (open symbols). Solid lines show the linear fitting results of each data with different cycle time. We also overplotted the coherence time calculation results using the same single source stare data as the fast switching simulation data, but for the data points with the baseline lengths longer than 1 km (filled symbols). Dashed lines are the linear fitting results of each data with different coherence time. Symbols are the same as in Fig. 3. Colors for the symbols and the fitted lines are the same as in Fig. 6.

using ALMA is currently ongoing (Asaki et al. 2014, 2016).

We also overplot in Fig. 7 (filled symbols) coherence as a function of coherence time, which is calculated as in the previous subsection (Sect. 3.3), using the same data sets as the fast switching simulation. Here, we set coherence to be the same as that of the fast switching simulation, and estimated coherence time. This will be useful once we know the difference between the coherence time and the simulated fast switching results, since the coherence time is easily calculated from the quick-look data (i.e., data taken for a short time, a minute or two, to check the quality of observational conditions), and it is possible to apply to the actual observations. The relation between coherence and coherence time is linear, and the fitting results are plotted in dashed lines. Comparison between the results of the fast switching calculations (open symbols) and that of the coherence time calculations (filled symbols) shows that the coherence time is almost always about 40-50% longer than in the fast switching simulation. This means that if we estimate the

coherence time from the quick-look data, then the recommended cycle time of an observation with fast switching will be about 40-50% shorter.

4. Summary

Using single source stare data taken during the ALMA long baseline campaigns carried out over the past 6 years, with baseline lengths of up to $\sim$ 15 km, we derived various atmospheric phase characteristics that will be useful for the ALMA long baseline (and high frequency) observations. The summary of our study is as follows:

- The 183 GHz WVR phase correction method works well for reducing the phase fluctuation at long baselines, especially for weather conditions with precipitable water vapor (PWV) larger than 1 mm.
- The WVR phase correction lengthens the coherence time by about a factor of two or more, indicating that the WVR phase correction is useful for lengthening the integration time and/or calibration time interval.
- The WVR phase correction, however, could not take out all the phase fluctuation, suggesting that there are other reasons that cause phase fluctuation at millimeter and submillimeter wavelengths. Combining other phase correction methods in addition to the WVR phase correction is important, such as the fast switching phase correction method.
- Indeed, our simulation of the fast switching phase correction method shows an improvement in the coherence of the data, especially with shorter cycle time than a few minutes.
- Most of the spatial structure functions (SSFs) of the data show one turn-over around a baseline length of 1 km. This result suggests that the scale height of the turbulent constituent is around 1 km, consistent with the distribution of water vapor. Combined with the success of the WVR phase correction, it is obvious that the main turbulent constituent is water vapor in the atmosphere.
- The fitted slopes indicate that most of the phase fluctuation at baseline lengths shorter than 1 km shows the intermediate value of theoretical 3-D and 2-D Kolmogorov turbulence (i.e., around 0.6), and that at baseline lengths longer than 1 km displays the intermediate value of theoretical 2-D Kolmogorov turbulence and no correlation (i.e., $0.2 - 0.3$).
- There are a few cases that do not show any turn-over. Such SSFs are only obtained under very low PWV conditions, when the improvement factor of the WVR phase correction is not high, or after the WVR phase correction. This suggests that the main turbulent constituent in these cases is not water vapor, and that the phase fluctuation caused by this constituent is inherently smaller than that caused by water vapor. The scale height of this constituent

is higher than 10 km, suggesting that water ice or a dry component (N_2 or O_2) can be the cause of the phase fluctuation.

- Excess path length fluctuation at a baseline length of 10 km is large, $\sim$ 200 μm even at PWV less than 1 mm (no large difference for the data before and after the WVR phase correction), and increases as a function of PWV. This value is significant for the high frequency observations, and strongly suggest to use other phase correction method, such as the fast switching and/or band-to-band phase correction methods.

This paper makes use of the following ALMA data: ADS/JAO.ALMA#0000.0.00341.CSV. ALMA is a partnership of ESO (representing its member states), NSF (USA) and NINS (Japan), together with NRC (Canada) and NSC and ASIAA (Taiwan), and KASI (Republic of Korea), in cooperation with the Republic of Chile. The Joint ALMA Observatory is operated by ESO, AUI/NRAO and NAOJ.

We express our gratitude to all the ALMA members for the support of the long baseline campaigns. SM and YA thank the Joint ALMA Observatory (JAO) for supporting our visit to ALMA as Expert Visitors in 2013 and 2014. SM and YA also expresses their appreciations to the National Astronomical Observatory of Japan (NAOJ) for their supports for their stays in Chile in 2012 – 2014. SM is supported by the National Science Council (NSC) and the Ministry of Science and Technology (MoST) of Taiwan, NSC 100-2112-M-001-006-MY3 and MoST 103-2112-M-001-032-MY3. LM and RT are part of the Dutch ALMA ARC node, Allegro, which is funded by the Netherlands Organisation for Scientific Research (NWO).

We deeply regret the loss of our colleague, Koh-Ichiro Morita, who lost his life on May 7th, 2012, at Santiago, Chile. He significantly helped not only this work but also for various works in the ALMA project, and without him, we could not achieve these results. Furthermore, he taught SM the basic and application of interferometry, phase correction methods, and site testings since SM was a graduate student at the Nobeyama Radio Observatory. Without his guidance, SM could not be at the current position. Morita-san, we really miss you...

A. Data List

Here, we present the list of the data used in this study. Data for the longest baseline lengths of 2 km, 3 km, and 10 – 15 km are shown in Tables 3, 4, and 5, respectively.

REFERENCES

ALMA Partnership, Fomalont, E. B., Vlahakis, C., et al. 2015, ApJ, 808, L1

Table 3. List of the 2 km baseline data used in this study.

Date	Time [UT]	Duration [min] [min]	ExecBlock	PWV [mm]	Band	Source	No. of BLs with ¿ 1 km
2012/05/02	11:02	20	uid__A002_X3f4b85_X392	1.54	6	1924-292	13
	11:28	20	uid__A002_X3f4b85_X399	1.65	6	1924-292	13
2012/05/10	04:22	20	uid__A002_X3ffc69_X71	0.98	6	3C279	14
	10:45	20	uid__A002_X401024_Xca	0.86	6	2258-279	13
	22:10	20	uid__A002_X401c5a_X13e	1.96	3	0522-364	16
2012/05/11	09:13	20	uid__A002_X403046_X3d	1.78	3	1924-292	14
2012/05/12	00:00	20	uid__A002_X404191_X26	1.91	3	3C279	16
	12:13	20	uid__A002_X4056cb_X3ac	1.14	3	3C454.3	13
	12:36	20	uid__A002_X4056cb_X3b3	1.30	7	3C454.3	13
2012/05/15	23:23	20	uid__A002_X40b03b_X2c	1.69	3	3C279	20
2012/05/16	01:29	20	uid__A002_X40b03b_X36c	1.56	3	3C279	19
	02:39	20	uid__A002_X40b03b_X465	1.46	3	3C279	18
	12:17	20	uid__A002_X40c17a_X120	0.69	3	3C454.3	18
2012/05/26	05:53	20	uid__A002_X412ad5_X5dd	1.97	3	1924-292	15

Table 4. List of the 3 km baseline data used in this study.

Date	Time [UT]	Duration [min] [min]	ExecBlock	PWV [mm]	Band	Source	No. of BLs with ¿ 1 km
2013/06/03	22:10	10	uid__A002_X65a644_Xd	0.68	3	1058+015	46
2013/06/06	05:59	10	uid__A002_X660b54_Xae2	0.54	3	NRAO530	49
	09:00	10	uid__A002_X660b54_X16de	0.55	3	1924-292	47
	11:12	10	uid__A002_X660b54_X1caf	0.55	3	2348-165	43
	11:33	10	uid__A002_X660b54_X1d7e	0.54	6	2348-165	43
	11:51	10	uid__A002_X660b54_X1f3c	0.57	7	2348-165	43
2013/06/07	05:24	10	uid__A002_X6643c8_X3e6	1.46	3	1924-292	53
	05:43	10	uid__A002_X6643c8_X425	1.42	6	1924-292	53
	06:00	10	uid__A002_X6643c8_X47d	1.39	7	1924-292	53

Table 5. List of the 10 – 15 km baseline data used in this study.

Date	Time [UT]	Duration [min] [min]	ExecBlock	PWV [mm]	Band	Source	No. of BLs with ¿ 1 km
2014/09/09	01:41	30	uid__A002_X8b5a69_Xd3	1.64	3	2253+1608	260
	02:17	30	uid__A002_X8b5a69_X233	1.45	7	2253+1608	260
2014/09/12	07:26	30	uid__A002_X8ba346_X9bb	1.89	3	0428-3756	222
2014/09/13	06:32	40	uid__A002_X8bc8aa_X962	2.53	3	0522-364	181
2014/09/14	09:25	40	uid__A002_X8bd3e8_Xa59	0.61	3	0522-364	259
	10:16	40	uid__A002_X8bd3e8_Xac6	0.57	6	0522-364	259
	11:22	40	uid__A002_X8bd3e8_Xc55	0.55	7	0522-364	245
2014/09/15	08:02	40	uid__A002_X8beb08_Xe43	0.95	3	0522-364	262
	08:50	40	uid__A002_X8beb08_Xea2	0.98	7	0522-364	262
2014/09/16	07:25	40	uid__A002_X8c0e65_Xc72	0.77	3	0522-364	278
	08:11	40	uid__A002_X8c0e65_Xe16	0.80	6	0522-364	265
	10:36	40	uid__A002_X8c0e65_X1151	0.75	7	0522-364	276
2014/09/23	01:29	40	uid__A002_X8d054c_X276	2.13	3	3C454.3	447
	05:00	40	uid__A002_X8d054c_X99b	1.95	6	3C454.3	360
	05:45	40	uid__A002_X8d054c_Xaf4	1.87	7	3C454.3	378
2014/09/26	23:51	30	uid__A002_X8d8bc2_Xe5	1.15	3	1924-292	378
2014/09/27	00:28	30	uid__A002_X8d8bc2_X125	1.05	6	1924-292	378
	01:08	30	uid__A002_X8d8bc2_X165	1.04	7	1924-292	378
	19:18	30	uid__A002_X8da59e_X5	1.48	3	1924-292	440
	19:53	30	uid__A002_X8da59e_X45	1.37	6	1924-292	440
	20:34	30	uid__A002_X8da59e_X85	1.54	3	1924-292	440
2014/09/28	16:21	30	uid__A002_X8dd128_X2b	1.00	3	3C279	191
2014/09/29	06:32	30	uid__A002_X8dd2a4_Xae7	0.59	8	0522-364	280
2014/10/01	05:27	30	uid__A002_X8e1004_Xec4	0.53	3	0522-364	400
	06:06	30	uid__A002_X8e1004_Xf04	0.53	6	0522-364	370
	06:43	30	uid__A002_X8e1004_Xf44	0.52	7	0522-364	400
	08:02	90	uid__A002_X8e1004_Xfe5	0.46	8	0522-3627	360
2014/10/05	09:37	30	uid__A002_X8ec7bb_X1123	0.33	3	0522-364	286
2014/10/29	23:06	30	uid__A002_X91bdc6_X36	1.94	3	3C454.3	410
2014/10/30	02:43	30	uid__A002_X91cc20_X8f	0.65	3	3C454.3	473
2014/11/01	19:04	30	uid__A002_X920302_X1d6d	1.33	3	1924-292	410

ALMA Partnership, Hunter, T. R., Kneissl, R., et al. 2015, ApJ, 808, L2

ALMA Partnership, Brogan, C. L., Pérez, L. M., et al. 2015, ApJ, 808, L3

ALMA Partnership, Vlahakis, C., Hunter, T. R., et al. 2015, ApJ, 808, L4

Asaki, Y., Matsushita, S., Fomalont, E. B., et al. 2016, Proc. SPIE, 9906, 99065U

Asaki, Y., Matsushita, S., Kawabe, R., Fomalont, E., Barkats, D., & Corder, S. A. 2014, Proc. SPIE, 9145, 91454K

Asaki, Y., Matsushita, S., Morita, K.-I., & Nikolic, B. 2012, Proc. SPIE, 8444, 84443K

Asaki, Y., Saito, M., Kawabe, R., Morita, K.-I., & Sasao, T. 1996, Radio Science, 31, 1615

Asaki, Y., Shibata, K. M., Kawabe, R., Roh, D.-G., Saito, M., Morita, K.-I., & Sasao, T. 1998, Radio Science, 33, 1297

Butler, B. J., Radford, S. J. E., Sakamoto, S., & Kohno, K. 2001, ALMA Memo, 365

Carilli, C. L., & Holdaway, M. A. 1999, Radio Science, 34, 817

Doeleman, S. S., Weintroub, J., Rogers, A. E. E., et al. 2008, Nature, 455, 78

Doeleman, S. S., Fish, V. L., Schenck, D. E., et al. 2012, Science, 338, 355

Dravskikh, A. F., & Finkelstein, A. M. 1979, Ap&SS, 60, 251

Hills, R. E., Kurz, R. J., & Peck, A. B. 2010, Proc. SPIE, 7733, 773317

Hufford, G. 1991, Intern. J. Infrared Millimeter Waves, 12, 677

Kameno, S., Nakai, N., & Honma, M. 2013, ASP Conf. Ser., 476, 409

Lay, O. P. 1997, A&AS, 122, 535

Liebe, H. J. 1989, Intern. J. Infrared Millimeter Waves, 10, 631

Liebe, H. J., Hufford, G. A., & Cotton, M. G. 1993, in AGARD 52nd Specialists' Meeting of the Electromagnetic Wave Propagation Panel, 3-1

Liebe, H. J., Hufford, G. A., & Manabe, T. 1991, Intern. J. Infrared Millimeter Waves, 12, 659

Matsushita, S., Asaki, Y., Fomalont, E. B., et al. 2016, Proc. SPIE, 9906, 99064X

Matsushita, S., Asaki, Y., Kawabe, R., Fomalont, E., Barkats, D., & Corder, S. A. 2014, Proc. SPIE, 9145, 91453I

Matsushita, S., & Chen, Y.-L. 2010, PASJ, 62, 1053

Matsushita, S., & Matsuo, H. 2003, PASJ, 55, 325

Matsushita, S., Matsuo, H., Sakamoto, A., & Pardo, J. R. 2000, Proc. SPIE, 4015, 378

Matsushita, S., Morita, K.-I., Barkats, D., Hills, R. E., Fomalont, E. B., & Nikolic, B. 2012, Proc. SPIE, 8444, 84443E

McMullin, J. P., Waters, B., Schiebel, D., Young, W., & Golap, K. 2007, ASP Conf. Ser., 376, 127

Morita, K.-I., Handa, K., Asaki, Y., Kitamura, Y., Yokogawa, S., Saito, M., Wilner, D. W., & Ho, P. T. P. 2000, ASP Conf. Ser., 217, 340

Nikolic, B., Bolton, R. C., Graves, S. F., Hills, R. E., & Richer, J. S. 2013, A&A, 552, 104

Nikolic, B., Graves, S. F., Bolton, R. C., & Richer, J. S. 2012, ALMA Memo, 593

Ray, P. S. 1972, Appl. Opt., 11, 1836

Remijan, A., Adams, M., & Warmels, R. 2015, ALMA Cycle 3 Technical Handbook

Sramek, R. A. 1990, Proceedings of the URSI/IAU Symposium on Radio Astronomical Seeing (Beijing/Oxford: International Academic Publishers/Pergamon Press), 21 (VLA Memo, 175)

Tatarskii, V. I. 1961, Wave Propagation in a Turbulent Medium (New York: Dover)

Taylor, G. I. 1938, Proc. Roy. Soc. London Ser. A, 164, 476

Thompson, A. R., Moran, J. M., & Swenson, G. W., Jr. 2001, Interferometry and Synthesis in Radio Astronomy (2nd ed.; New York: Wiley-Interscience)

Treuhaft, R. N., & Lanyi, G. E. 1987, Radio Science, 22, 251

Wiedner, M. C., Hills, R. E., Carlstrom, J. E., & Lay, O. P. 2001, ApJ, 553, 1036

Wright, W. C. H. 1996, PASP, 108, 520